



Simulation and experiment investigations on fabrication of Fe-based amorphous powders by a novel atomization process equipped with assisted gas nozzles

Jia-qi Liu¹ · Yan-nan Dong¹ · Pu Wang¹ · Huan Zhao² · Jing Pang² · Xiao-yu Li² · Jia-quan Zhang¹

Received: 9 June 2022 / Revised: 2 September 2022 / Accepted: 5 September 2022 / Published online: 27 September 2022
© China Iron and Steel Research Institute Group 2022

Abstract

Based on computational fluid dynamics method, the effect of atomization gas pressure on the atomization efficiency of Laval nozzle was studied, and then a discrete phase model was established and combined with industrial trials to study the effect of a new type of assisted gas nozzles (AGNs) on powder size distribution and amorphous powder yield. The results show that increasing the atomization pressure can effectively improve the gas velocity for the Laval nozzle; however, it will decrease the aspiration pressure, and the optimal atomization pressure is 2.0 MPa. Compared with this, after the application of AGNs with the inlet velocity of 200 m s^{-1} , assisted gas jet can increase the velocity of overall droplets in the break-up and solidification area by 40 m s^{-1} and the maximum cooling rate is increased from 1.9×10^4 to $2.3 \times 10^4 \text{ K s}^{-1}$. The predicted particle behavior is demonstrated by the industrial trails, that is, after the application of AGNs, the median diameter of powders d_{50} is decreased from 28.42 to 25.56 μm , the sphericity is increased from 0.874 to 0.927, the fraction of amorphous powders is increased from 90.4% to 99.4%, and only the coercivity is increased slightly due to the accumulation of internal stress. It is illustrated that the AGNs can improve the yield of fine amorphous powders, which is beneficial to providing high-performance raw powders for additive manufacturing technology.

Keywords Computational fluid dynamics · Atomization · Assisted gas nozzle · Discrete phase model · Amorphous powder

1 Introduction

Additive manufacturing (AM) is a rapid forming technology based on discrete materials such as powders and wires to prepare parts through layer-by-layer stacking, which has been widely used in high-end electronics, medical devices and aerospace fields with unique advantages, e.g., precision processability, fast manufacturing speed and low energy consumption [1, 2]. At present, under the strategic goal of “low carbon, energy saving and emission reduction”, integration,

miniaturization and high-frequency are the inevitable development trends of electronic equipment [3–5]. Fe-based amorphous alloys have become a new generation of soft magnetic materials due to their excellent comprehensive properties such as low cost, high saturation magnetization, low coercivity and low high-frequency core loss [6]. Due to the limitation of the glass forming ability of Fe-based amorphous systems, powder metallurgy process is often used to produce Fe-based amorphous powders with high cooling rate requirements, and then bulk metallic glasses are prepared by subsequent consolidation processes [7–9]. Therefore, AM technology that can break through the size and shape limitations of bulk metallic glasses is expected to be a key technology for solving the preparation of large-sized and complex-shaped amorphous parts in the future [10].

The characteristics of raw powders have an important impact on the performance of the parts, e.g., the melting uniformity of powders is related to powder size, the density of the parts is related to powder sphericity, and the purity of the parts is related to powder purity. Therefore, raw powders

✉ Pu Wang
wangpu_ustb@163.com

✉ Jia-quan Zhang
jqzhang@metal.ustb.edu.cn

¹ School of Metallurgical and Ecological Engineering,
University of Science and Technology Beijing,
Beijing 100083, China

² Qingdao Yunlu Advanced Materials Technology Co., Ltd.,
Qingdao 266232, Shandong, China

with fine particle size, high purity and high sphericity are required by the preparation of high-quality parts. The characteristics of powders are significantly affected by different powder fabrication processes [8, 11, 12]. Mechanically alloying and strip crushing methods are two common processes for fabricating amorphous powders; however, the powders produced by these two methods have irregular shape with sharp edges, which easily lead to magnetic anisotropy and are unfavorable for subsequent processing [13]. Although the water atomization method has a high cooling rate (up to 10^4 K s^{-1} or more), the droplets are prone to oxidation and spheroidize insufficiently due to too rapid solidification, and the powder sphericity and purity are poor [14–16]. Compared with the above processes, the gas atomization and gas–water combined atomization, which have sufficient cooling rate, low cost and excellent powder characteristics, have become the main processes for fabricating Fe-based amorphous powders, and the relevant studies have been extensively reported in recent years.

Aydin and Unal [17] investigated the melt delivery tube tip base pressure and flow separation phenomenon for the close-coupled nozzle system. They verified the accuracy of computational fluid dynamics (CFD) for predicting the atomization efficiency and optimizing the nozzle geometry parameters, and found that a reasonable gas nozzle design can effectively avoid the flow separation phenomena. Ouyang et al. [18] studied the effect of melt superheat on the break-up process and found that the increase in melt superheat could reduce the thickness of melt liquid film during primary atomization and the powder size after secondary atomization. Schwenck et al. [19] designed a new annular slit Laval nozzle and investigated its atomization behavior under different atomization process parameters by numerical simulation and high-speed imaging technology. Thompson et al. [20] quantitatively investigated the effect of industrial close-coupled gas nozzle geometry and atomization process parameters on powder size distribution by discrete phase model (DPM) and found that increasing atomization gas pressure and decreasing melt surface tension can effectively reduce powder size. Wang et al. [21] conducted an integral simulation for vacuum induction gas atomization with close-coupled nozzle, and the powder size after secondary atomization was in good agreement with the experimental results. In addition, they found that the evolution process of spherical and irregularly shaped powders during the atomization, and suggested that reasonable optimization of the atomization flow field and control of the gas jet can effectively promote the formation of spherical powders. Shi et al. [8] used realizable $k-\varepsilon$ turbulence model with DPM to simulate the gas atomization process of Fe-based amorphous powders under different atomization pressures and summarized the effect of atomization pressure on powder properties by combining with the characterization of powders. Luo

et al. [22] reproduced the specific details of droplet break-up and defect evolution during gas atomization by combining the dynamic adaptive mesh, volume of fluid model and DPM, and proposed feasible initiatives to improve the powder yield. Ciftci et al. [23] investigated the effect of different gas temperatures on gas atomization, and the results showed that hot gas atomization can significantly improve the yield of amorphous powders, although it has little effect on the cooling rate.

In recent years, the research on the flow field of gas atomization, break-up mechanism during primary atomization and secondary atomization has been widely reported, but the study about new industrial atomization equipment is mostly limited to the structural optimization of nozzles and delivery tubes, and the research on new atomization equipment and process is rare. Based on this, a flow-heat transfer model of atomization gas-only flow field was established in this study. Firstly, the flow field characteristics of the Laval nozzle under different atomization pressures were analyzed, and the appropriate atomization pressure for the nozzle was discussed. Then, a one-way coupling DPM was established and combined with industrial trials to study the effect of a novel type of assisted gas nozzles (AGNs) on the yield of spherical amorphous fine powders. Finally, the effects of AGNs on the size, sphericity, amorphous fraction and soft magnetic properties of powders were compared by the characterization of powders to provide theoretical and practical guidance for the development of novel atomization equipment and processes.

2 Numerical and experimental methods

2.1 Model assumption and governing equations

In this study, the steady-state simulation of the gas-only flow field inside the industrial atomization chamber was calculated by Fluent 19.1 which is a commercial CFD software based on the finite volume method, and a DPM was developed to analyze the effect of AGNs on the powder particles. Under the premise of ensuring the calculation accuracy, the following assumptions were made to simplify the actual physical problems and save computational resources:

- (i) The Mach number of gas jet flow during atomization is less than 0.3, and therefore, the atomization gas N_2 can be treated as a compressible fluid conforming to the ideal gas law [21];
- (ii) The walls of the atomization chamber, nozzles and the delivery tube are all considered to be adiabatic and smooth non-slip walls;
- (iii) Considering the symmetry of the atomization chamber structure, it is assumed that the actual

internal gas flow field exhibits axisymmetric, and then the three-dimensional model can be simplified into a two-dimensional axisymmetric model;

- (iv) In actual atomization production, the mass of molten steel injected in each batch is small, so that only the effect of N₂ on particles is considered, and the mass loading effect of particles on N₂ is ignored in this model;
- (v) Only liquid metal droplets are considered, and the break-up and agglomeration of droplets during the atomization are ignored.

Based on the above analysis, the steady-state gas-only flow field of the compressible fluid in the two-dimensional axisymmetric geometric model satisfies the following governing equations [17, 22, 24]:

Mass conservation equations:

$$\frac{\partial}{\partial x}(\rho v_x) + \frac{\partial}{\partial r}(\rho v_r) + \frac{\rho v_r}{r} = S_m \tag{1}$$

where x is the axial coordinate; ρ is the density of N₂, and according to the ideal gas law, ρ is given by $\rho = \frac{P_{op} + P}{M_w T}$; P_{op} is the operating pressure value (set to 101 kPa); P is the local static pressure; R is the universal gas constant; M_w is the molecular weight; T is the local temperature; v_x is the axial velocity; r is the radial coordinate; v_r is the radial velocity; and S_m is the mass added to the continuous phase N₂ from the discrete particles.

Momentum conservation equations:

$$\frac{1}{r} \frac{\partial}{\partial x}(r \rho v_x v_x) + \frac{1}{r} \frac{\partial}{\partial r}(r \rho v_r v_x) = -\frac{\partial P}{\partial x} + \frac{1}{r} \frac{\partial}{\partial x} \left[r \mu \left(2 \frac{\partial v_x}{\partial x} - \frac{2}{3} (\nabla \cdot \vec{v}) \right) \right] + \frac{1}{r} \frac{\partial}{\partial r} \left[r \mu \left(\frac{\partial v_x}{\partial r} + \frac{\partial v_r}{\partial x} \right) \right] + F_x \tag{2}$$

$$\frac{1}{r} \frac{\partial}{\partial x}(r \rho v_x v_r) + \frac{1}{r} \frac{\partial}{\partial r}(r \rho v_r v_r) = -\frac{\partial P}{\partial r} + \frac{1}{r} \frac{\partial}{\partial x} \left[r \mu \left(\frac{\partial v_r}{\partial x} + \frac{\partial v_x}{\partial r} \right) \right] + \frac{1}{r} \frac{\partial}{\partial r} \left[r \mu \left(2 \frac{\partial v_r}{\partial r} - \frac{2}{3} (\nabla \cdot \vec{v}) \right) \right] - 2\mu \frac{v_r}{r^2} + \frac{2\mu}{3r} (\nabla \cdot \vec{v}) + \rho \frac{v_z^2}{r} + F_r \tag{3}$$

$$\nabla \cdot \vec{v} = \frac{\partial v_x}{\partial x} + \frac{\partial v_r}{\partial r} + \frac{v_r}{r} \tag{4}$$

where μ is the molecular viscosity; F_x and F_r is axial and radial body forces, respectively; \vec{v} is the velocity vector; and v_z is the swirl velocity.

Energy conservation equations:

$$\rho \frac{\partial E}{\partial t} + \rho \nabla \cdot (H \vec{v}) = \nabla \cdot (\bar{\tau} \vec{v}) - \nabla \cdot \vec{q} \tag{5}$$

where E is the total energy; t is the time; H is the enthalpy; $\bar{\tau}$ is the stress tensor; and \vec{q} is the heat flux vector.

SST $k-\omega$ turbulence equations:

$$\nabla \cdot (\rho k \vec{v}) = \nabla \cdot (\Gamma_k \nabla \cdot k) + G_k - Y_k + S_k \tag{6}$$

$$\nabla \cdot (\rho \omega \vec{v}) = \nabla \cdot (\Gamma_\omega \nabla \cdot \omega) + G_\omega - Y_\omega + S_\omega + D_\omega \tag{7}$$

where k is the turbulent energy; ω is the special turbulence dissipation; Γ_k and Γ_ω are the effective diffusivities of k and ω , respectively; G_k and G_ω is the production of k and ω , respectively; Y_k and Y_ω are the dissipation of k and ω , respectively; S_k and S_ω are user-defined source terms; and D_ω is the cross-diffusion term.

Particle force balance equation in DPM:

$$m_p \frac{d\vec{u}_p}{dt} = m_p \frac{\vec{u} - \vec{u}_p}{\tau_r} + m_p \frac{\vec{g}(\rho_p - \rho)}{\rho_p} \tag{8}$$

where m_p is the particle mass; \vec{u} is the N₂ velocity; \vec{u}_p is the particle velocity; ρ_p is the particle density; $m_p \frac{\vec{u} - \vec{u}_p}{\tau_r}$ is the drag force; \vec{g} is the graviton; and τ_r is the particle relaxation time calculated by:

$$\tau_r = \frac{\rho_p d_p^2}{18\mu C_d Re} \tag{9}$$

where d_p is the particle diameter; C_d is the drag coefficient; and Re is the relative Reynolds number, which is defined as follows:

$$Re = \frac{\rho d_p |\vec{u}_p - \vec{u}|}{\mu} \tag{10}$$

2.2 Boundary condition and solution modes

The schematic diagram of the location of AGNs is shown in Fig. 1a, and the AGNs are cylindrical nozzles with a diameter of 4 mm. The angle between the nozzle and the vertical direction is 10°, and the distance between the nozzle and the outlet of the delivery tube and the distance between the nozzle and the central axis are all 150 mm. The mesh and boundary conditions of the atomization equipment used in this study are shown in Fig. 1b, where the boundary conditions used for DPM simulation are the same as those in the gas-only flow field calculation. The atomization gas nozzle is set as the pressure inlet, the AGN is set as the velocity inlet, the left boundary and the lower boundary of the atomization chamber are set as the pressure outlet, the central axis is set as the axis, and the rest are set as the wall. The size of the overall computational domain is 1100 mm × 300 mm, and the mesh refinement is adopted near the nozzles and the central area of the atomization chamber with large gradients of physical

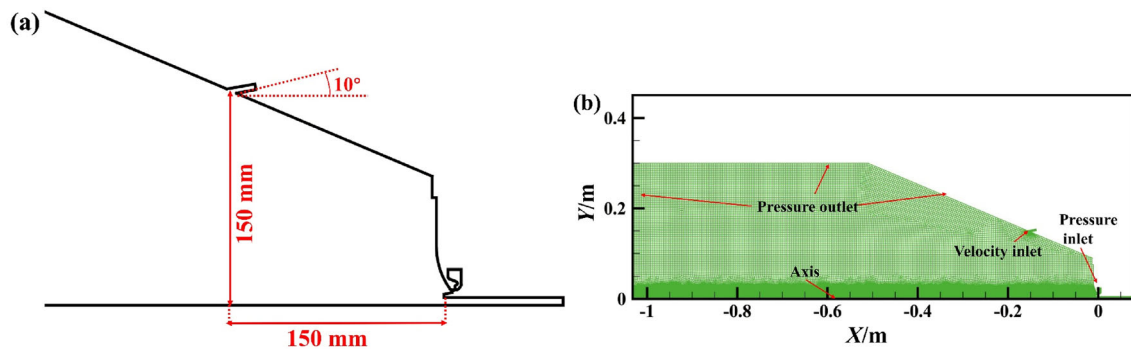


Fig. 1 Schematic diagram of AGN position (a) and two-dimensional axisymmetric mesh and boundary conditions (b)

quantities. The minimum mesh size is 0.25 mm, and the mesh type is quadrilateral.

Based on the research of Salvador et al. [25] research about the computational accuracy of different turbulence models in the spraying process, the SST $k-\omega$ turbulence model with higher accuracy for the development of internal flow and atomization gas jet was selected in this study. During the process of model solving, the characteristics of gas-only flow field for the Laval nozzle under different atomization gas pressures were firstly calculated without AGNs, and then the variation of the flow field in the atomization chamber was compared under different inlet gas velocities of AGNs. Considering that it was difficult to analyze the overall characteristics of the flow field due to the large-sized domain, after the gas-only flow field was solved to convergence, the one-way coupling DPM was applied to more intuitively observe the flow field variation with and without AGNs. In this study, N_2 was the continuous phase and the metal droplet was the discrete phase. Based on the study by Markus et al. [26] and our previous primary atomization calculations, the injection was released from the delivery tube tip. The mass flow rate of particles was 0.05 kg s^{-1} , the initial velocity magnitude of particles was 2.2 m s^{-1} , the temperature of particles was 1573 K, and the particle size distribution was in the range of 0.1–1.0 mm that obeyed the Rosin–Rammler

distribution. The material parameters of N_2 and metal droplets and other process parameters used in the calculation are shown in Table 1.

In the solution process, the coupled scheme was adopted as the pressure–velocity coupling scheme, the pressure was discretized in the standard, the momentum, swirl velocity, turbulent velocity, turbulent kinetic energy, specific dissipation rate and energy were discretized in the second order upwind. The residuals of continuity and energy equation were set as 10^{-5} and 10^{-6} , respectively, and other residuals were set as 10^{-4} .

2.3 Mesh independence and model validation

First, four meshes with nodes of 42,646, 78,636, 183,705 and 320,585 were used to investigate the effect of mesh numbers on the simulation results, and the gas-only flow field without AGNs was solved to convergence under 2.0 MPa atomization pressure. The velocity magnitude at the characteristic point (-0.01 m , 0.005 m) below the delivery tube is shown in Fig. 2. When the mesh number is less than 183,705, the velocity at the characteristic point changes greatly with the increase in the mesh number, and as the mesh number further increases, its influence on the flow field gradually weakens. Therefore, considering the

Table 1 Geometry and material properties for numerical simulation

Parameter	Value	Parameter	Value
Density of N_2 /(kg m^{-3})	Ideal-gas	Density of droplets/(kg m^{-3})	7175
Specific heat of N_2 /($\text{J kg}^{-1} \text{K}^{-1}$)	1040.67	Specific heat of droplets/($\text{J kg}^{-1} \text{K}^{-1}$)	1350
Thermal conductivity of N_2 /($\text{J kg}^{-1} \text{m}^{-1}$)	0.0242	Thermal conductivity of droplets/($\text{J kg}^{-1} \text{m}^{-1}$)	42
Viscosity of N_2 /($\text{kg m}^{-1} \text{s}^{-1}$)	Sutherland	Temperature of N_2 /K	300
Temperature of droplets/K	1573	Delivery tube diameter/mm	2.0
Atomization gas pressure/MPa	0.5, 1.0, 1.5, 2.0, 2.5, 3.0	Inlet gas velocity of AGNs/(m s^{-1})	0, 50, 100, 150, 200

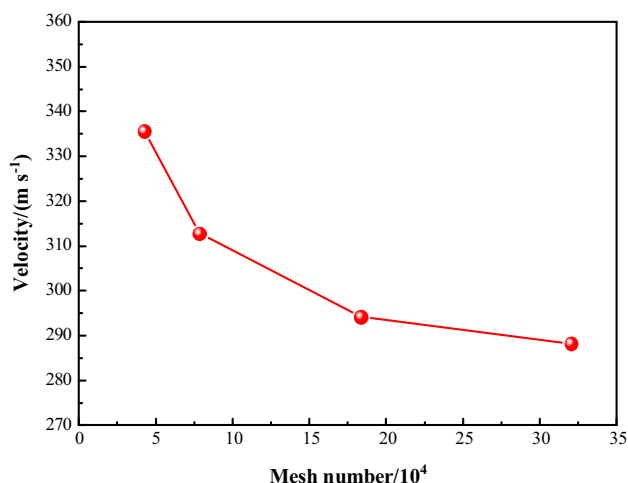


Fig. 2 Comparison of velocity at point (− 0.01 m, 0.005 m) under different mesh numbers

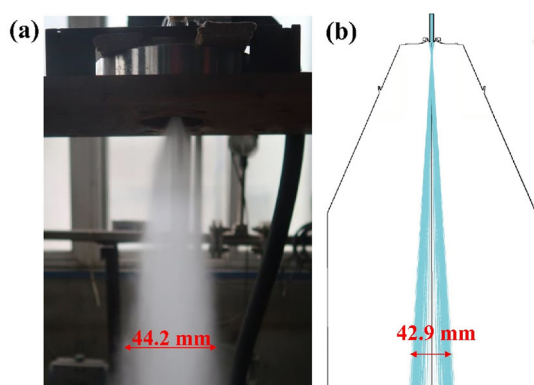


Fig. 3 Results of atomization trials (a) and simulation (b)

computational resources and accuracy, the mesh with 183,705 nodes was used for calculation in this study.

To validate the model and assumptions, an industrial trial was conducted as shown in Fig. 3a. The atomization gas pressure was 1.0 MPa, the atomization gas was N₂, the high-temperature melt was replaced by water for visualizing the atomization process, and the final measured scattering width at the position 100 mm from the outlet was 44.2 mm. Based on the above model and boundary conditions, the gas-only flow field at 1.0 MPa atomization pressure was calculated to convergence, and then the one-way coupling DPM was applied for calculation. The results are shown in Fig. 3b, and the scattering width at the same position is 42.9 mm, which is only 2.9% in error with the trial results, indicating the applicability of the model for predicting the flow field development and particle trajectory in the atomization process.

2.4 Experimental procedure

Commercial iron (purity > 99.9%), silicon (purity > 99.5%), boron (purity > 99.9%) and pre-alloyed Fe–B and Fe–C alloys were used as raw materials and mixed to the powder nominal composition Fe_{70.8}Si_{11.4}B_{11.9}C_{3.2}Cr_{2.7} (at.%). The powders were fabricated separately by the above novel atomization process under the conditions of without AGNs and with 200 m s⁻¹ inlet velocity of AGNs, and then the powders were dehydrated, dried and sieved to obtain the finished products (powder A and powder B are used to represent these two kinds of powders in this paper). The gas nozzle was a Laval nozzle (convergent–divergent nozzle), throat diameter was 0.34 mm, the capacity of crucible was 15 kg, the atomization gas pressure was 2.0 MPa, and the AGNs were arranged symmetrically on the left and right sides of the atomization chamber.

The morphology of the powders was observed using the Phenom Pro Desktop scanning electron microscope (SEM), and the accelerating voltage is 10 kV [27]. The sphericity of the powders was counted by Phenom Prisuite Software. The particle size distribution of the atomization powders was measured by the BT-9300S laser diffraction particle size analyzer (the detection particle size range was 0.1–341 μm, the shading rate was set as 16.02%, the refractive index of the medium was set as 1.333, and the refractive index of the sample was set as 2.860). The D2 Phaser X-ray diffractometry (XRD) was used to characterize the structure of the powders (Cu Kα, λ = 0.154184 nm). The step size was 0.02°, the scanning range was 20°–100°, the tube voltage was 30 kV and tube current was 10 mA. The crystallization enthalpy of the powders was measured by the SETSYS-1750 CS Evol-TG-DSC 1600 K differential scanning calorimeter (DSC) at a heating rate of 10 and a 30 mL min⁻¹ flow rate of high purity argon, and then the influence of the AGNs on the yield of amorphous powders was analyzed. Simultaneously, the crystallization enthalpy of powder B sieved to different size ranges was also measured by the same condition to characterize the effect of particle size on the fraction of amorphous powders. The saturation magnetization and coercivity of the powders were measured by Lake Shore 8604 vibrating sample magnetometer at the maximum applied magnetic field intensity of ± 8.0 × 10⁵ and ± 1.6 × 10⁴ A m⁻¹, respectively.

3 Results and discussion

3.1 Effect of atomization pressure on flow field without AGNs

As shown in Fig. 4a, b, when the atomization pressure is 2 MPa, the jet flow is ejected from the throat through the convergent part of the Laval nozzle and then rapidly expands and accelerates to supersonic speed. According to the law of isentropic flows, the pressure and temperature decrease rapidly (consistent with the characteristics in Fig. 4c, d), and then a series of Prandtl–Meyer waves are formed below the nozzle outlet under the action of the pressure difference. Subsequently, the jet repeats periodic expansion and contraction through continuous Prandtl–Meyer wave and oblique shocks (manifested as pressure fluctuations below the delivery tube tip in Fig. 4d) until its pressure equals to the ambient pressure and the flow field tends to be stable. In addition, at the wake region of jet intersection below the delivery tube tip, a typical recirculation zone is formed due to the deflection of gas flow path [28]. In the recirculation zone, the upward gas flow approaches the delivery tube tip and then extends radially until the gas flow touches the sonic boundary, and returns to the initial position of the recirculation zone under the action of the gas jet with high kinetic energy to complete a recirculation process. In this process, part of the subsonic

gas flows out of the recirculation zone, and part of the supersonic gas crosses the sonic boundary and enters the recirculation zone due to energy loss, and the flow difference between the two determines whether the pressure below the delivery tube tip is positive or negative [21]. Unal [29] proposed that ensuring a high negative pressure value below the delivery tube is of great significance to promote the smooth atomization and improve the atomization efficiency. If a high positive pressure field exists below the delivery tube, the downward flow of melt will be hindered and extend in the radial direction, and then the melt is easy to solidify under the cooling effect of the low-temperature gas jet near the nozzle outlet (Fig. 4b), which may change the shape of delivery tube and even cause freeze off [11, 17]. Therefore, under the premise of ensuring the atomization efficiency, the freeze off and flow separation phenomenon must be avoided by applying a reasonable atomization pressure, gas nozzle and delivery tube structure for the antegrade atomization process, which is important to keep the smooth atomization process [17, 19].

Figure 5a, b is the curves of pressure and axial velocity magnitude on the X-axis under different atomization pressures without AGNs, respectively. The two curves show opposite trends and conform to the characteristics of the atomization flow field of typical Laval nozzles [30]. For the gas nozzle in this study, the aspiration pressure below the

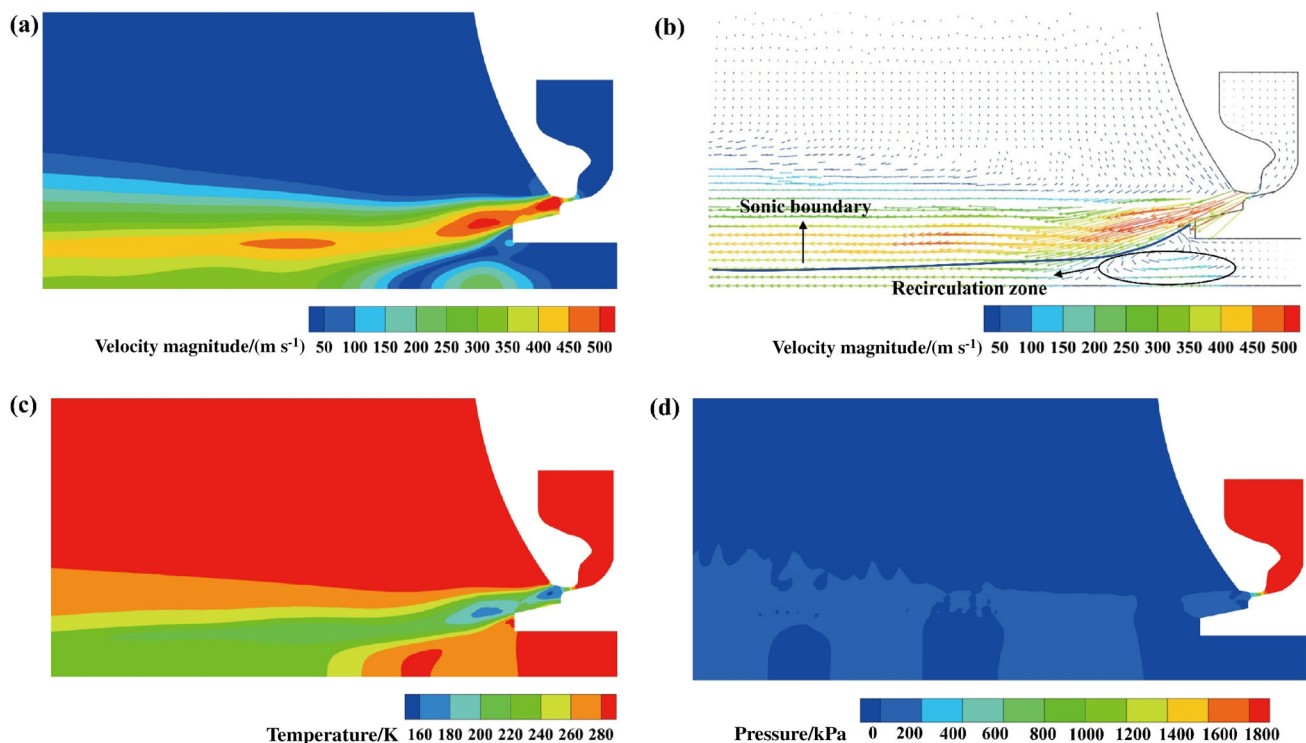


Fig. 4 Distribution of velocity magnitude (a), velocity vector (b), temperature (c) and pressure (d) under condition of 2.0 MPa atomization pressure without AGNs

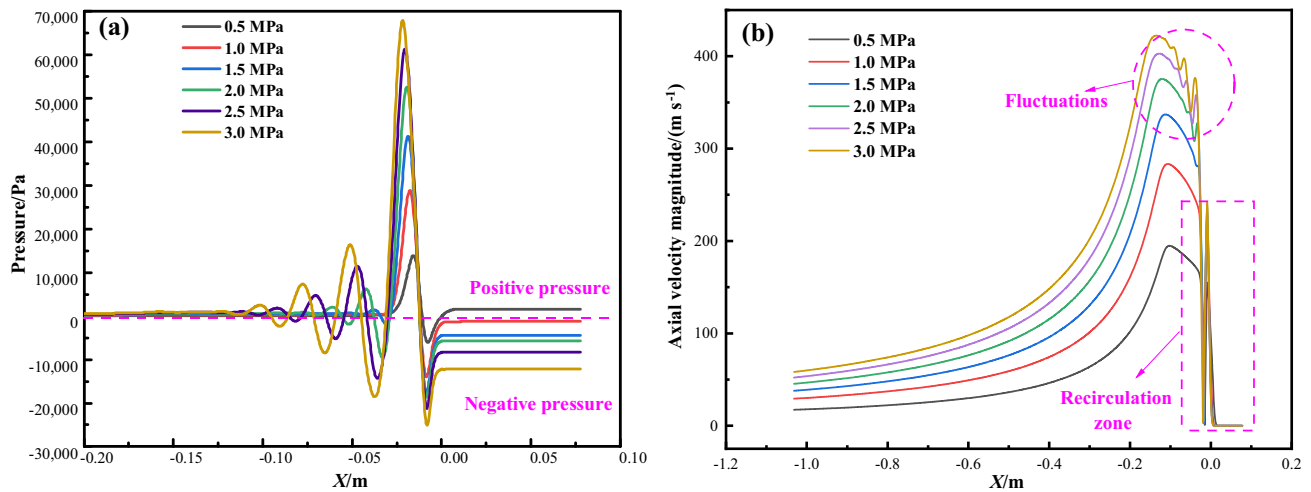


Fig. 5 Distribution curves of pressure **(a)** and axial velocity magnitude **(b)** on X -axis under condition of 2.0 MPa atomization pressure without AGNs

delivery tube tip decreases with the increase in atomization pressure, gradually decreasing from 1609.8 Pa at 0.5 MPa to $-12,180.3$ Pa at 3.0 MPa, which indicates that increasing the atomization pressure is conducive to promoting the downward flow of the melt. In addition, as the atomization pressure increases from 0.5 to 3.0 MPa, the maximum velocity in the recirculation zone increases from 154.9 to 240.2 m s^{-1} and the maximum velocity in the atomization chamber increases from 194.9 to 422.3 m s^{-1} . However, the intensity of shocks also increases with the atomization pressure, which leads to drastic fluctuations of pressure and velocity, and the energy conversion efficiency between gas and melt decreases [11]. Moreover, excessive negative pressure value will make melt downflow too fast, which will cause insufficient break-up and is not conducive to improving the yield of fine powders [30]. Therefore, the atomization pressure of about 2.0 MPa is selected in actual

industrial production, which is consistent with the simulation results.

3.2 Influence of inlet velocity for AGNs on flow field

To study the effect of the inlet gas velocity of AGNs on the atomization flow field, four velocities of 50, 100, 150 and 200 m s^{-1} are simulated in combination with the actual industrial conditions. Figures 6 and 7 are the temperature and velocity distribution under different inlet velocities, respectively. After the application of AGNs, the velocity of the assisted gas jet is continuously attenuated after leaving the nozzle, and the kinetic energy of the gas is converted into heat energy, resulting in an increase in the temperature near the nozzle outlet. With the increase in the inlet velocity, the high-temperature area gradually extends along

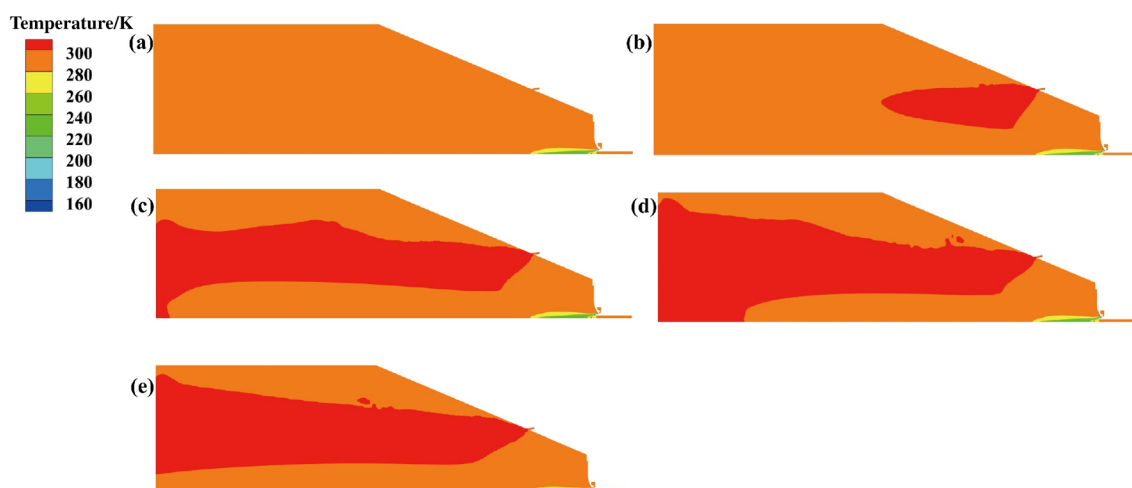


Fig. 6 Distribution of temperature under different inlet velocities for AGNs. **a** 0 m s^{-1} ; **b** 50 m s^{-1} ; **c** 100 m s^{-1} ; **d** 150 m s^{-1} ; **e** 200 m s^{-1}

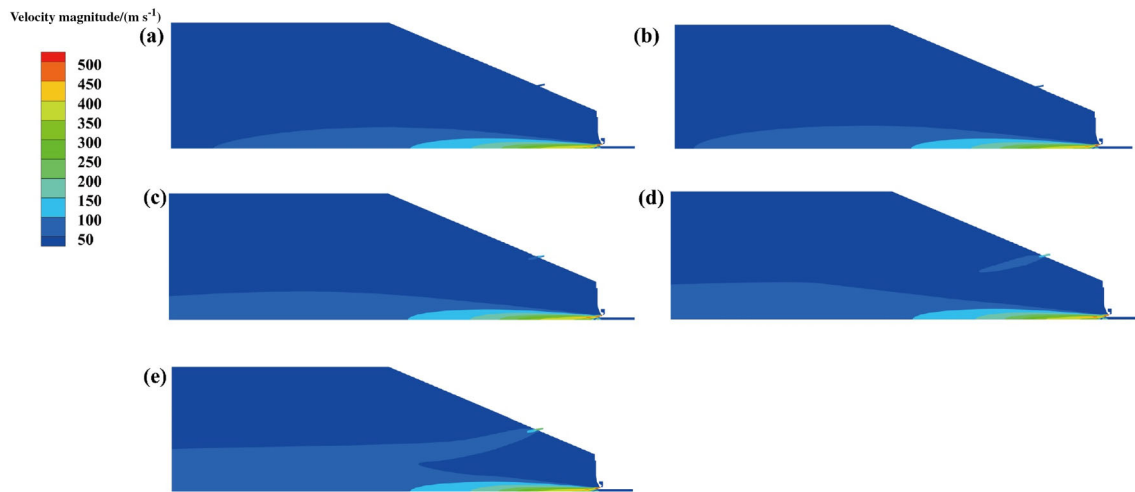


Fig. 7 Distribution of velocity under different inlet velocities for AGNs. **a** 0 m s^{-1} ; **b** 50 m s^{-1} ; **c** 100 m s^{-1} ; **d** 150 m s^{-1} ; **e** 200 m s^{-1}

the nozzle outlet to the area in the lower part of the atomization chamber. For the velocity distribution (Fig. 7), when the inlet velocity is low (Fig. 7b, c), the shape of the velocity contour does not change significantly except that the jet penetration ability is slightly enhanced; when the inlet velocity is increased to more than 150 m s^{-1} , the velocity of the flow field near the AGNs and bottom of the atomization chamber is increased significantly.

The curves of pressure and axial velocity magnitude on the X-axis under different inlet velocities of AGNs are shown in Fig. 8a, b, respectively. For the pressure curve after applying AGNs, a small pressure peak is formed in the range of -0.2 to 0.5 m on the X-axis (just below the AGNs), and after reaching the peak, the pressure decays to the value without AGNs. With the increase in the inlet gas velocity, the kinetic energy of the gas increases, and the pressure peak value and range increase. It can be seen from Fig. 8b that with the increase in inlet velocity, the attenuation of the gas velocity decreases. After applying AGNs with the inlet velocity of 200 m s^{-1} , the velocity of the flow field in the lower part of the atomization chamber increased from 45.4 m s^{-1} without AGNs to 70.4 m s^{-1} . Based on the above discussion, considering the limitations of industrial equipment, the selection of 200 m s^{-1} inlet velocity is selected for subsequent discussion. The velocity vector diagram without or with 200 m s^{-1} inlet velocity of AGNs is shown in Fig. 9a, b, respectively. Without AGNs, the gas flow velocity has been greatly attenuated near the AGNs, and the overall velocity is less than 50 m s^{-1} . After the application of AGNs, although the jet velocity does not accelerate to supersonic speed and gradually decays due to the structural characteristics of the cylindrical nozzle for AGNs, the gas flow velocity and direction near the AGNs are still significantly improved. In Sect. 3.3, a DPM will be used to reflect the change of atomization efficiency more

intuitively with or without AGNs through particle information.

3.3 Comparison of atomization efficiency before and after application of AGNs

Considering the motion trajectories of the actual particles, a one-way coupling DPM is applied on the basis of the above steady-state calculation results of gas-only flow field to more clearly reflect the influence of the AGNs on the flow field. The distribution of particle velocity and diameter without AGNs and with the inlet velocity of 200 m s^{-1} for AGNs are shown in Fig. 10a, b, respectively. Without AGNs, the maximum particle velocity is 169.8 m s^{-1} , and the particle dispersion angle is 12.8° . After applying AGNs with the inlet velocity of 200 m s^{-1} , the assisted jet flow increases the kinetic energy of the particles, which increases the maximum particle velocity to 202.2 m s^{-1} . In addition, the particles are more concentrated under the action of the assisted jet flow, and then the dispersion angle is reduced from 12.8° to 9.0° . It can be seen from Fig. 10b that without AGNs, the large droplets are located in the middle of the atomizing cone due to large inertia, and the small droplets are dispersed to the periphery of the atomizing cone due to small inertia under the impact of the jet. After applying AGNs, the distribution of droplets is similar to that without AGNs, but some small droplets on the periphery move to the middle under the action of assisted jet flow, which is the reason for the decrease of the dispersion angle.

Under the conditions of without AGNs and with 200 m s^{-1} inlet velocity of AGNs, the fitting curves of droplet diameter-velocity and droplet diameter-temperature at $X = -0.3 \text{ m}$ are shown in Fig. 11a, b, respectively. Since small droplets have larger acceleration, the droplet

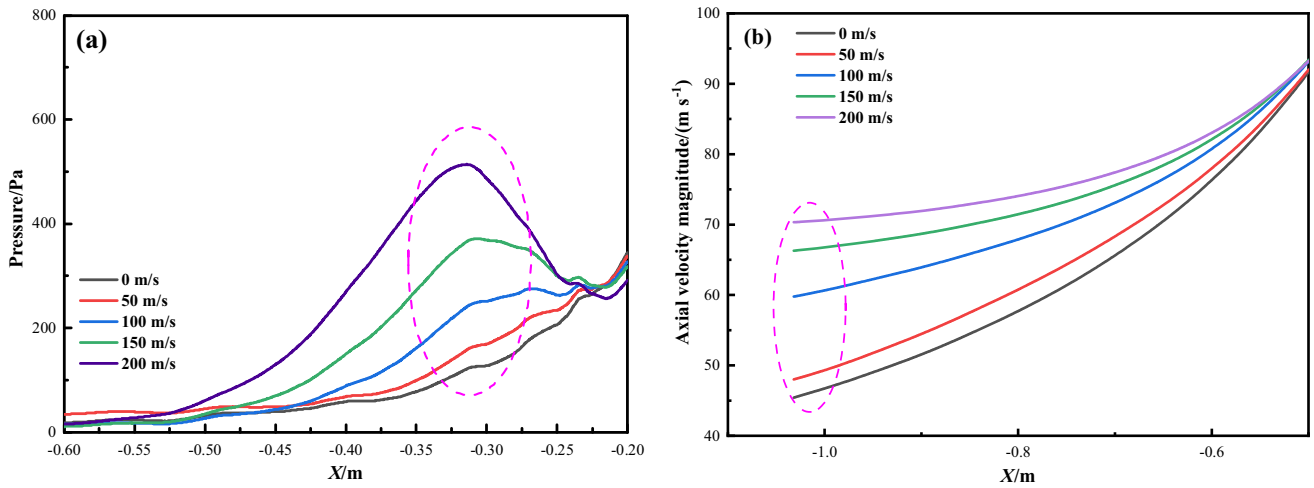


Fig. 8 Distribution curves of pressure (a) and axial velocity magnitude (b) on X-axis under different inlet velocities for AGNs

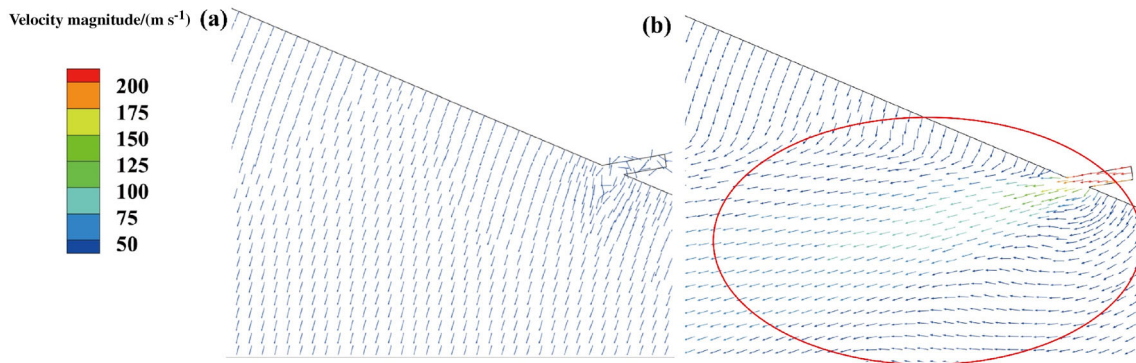


Fig. 9 Diagram of velocity vector near AGNs. a Without AGNs; b with 200 m s^{-1} inlet velocity of AGNs

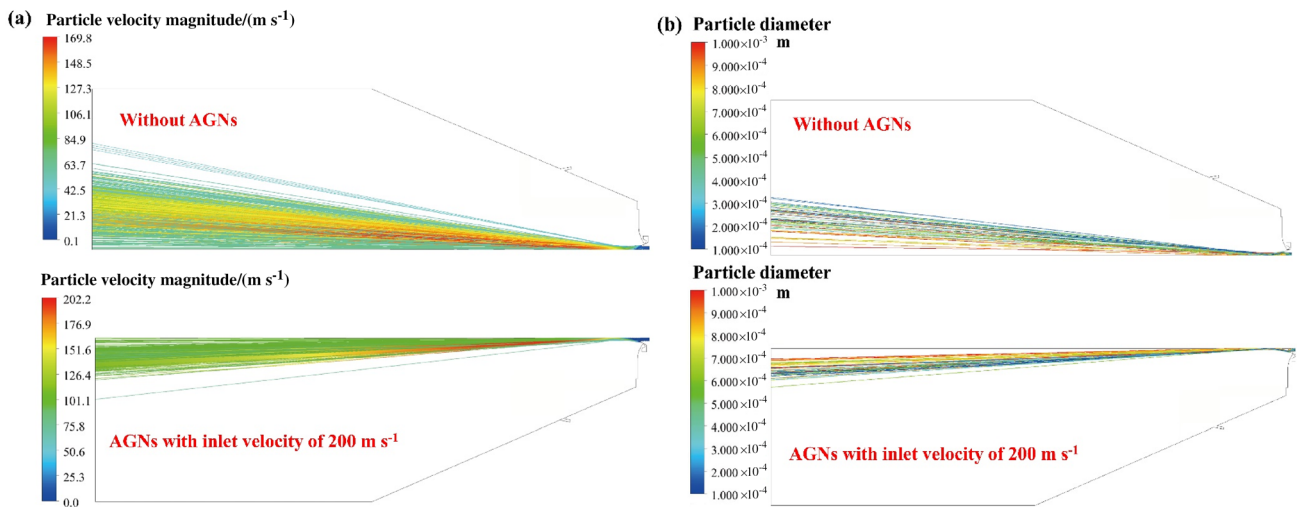


Fig. 10 Distribution of particle velocity (a) and particle diameter (b) without AGNs and with 200 m s^{-1} inlet velocity of AGNs

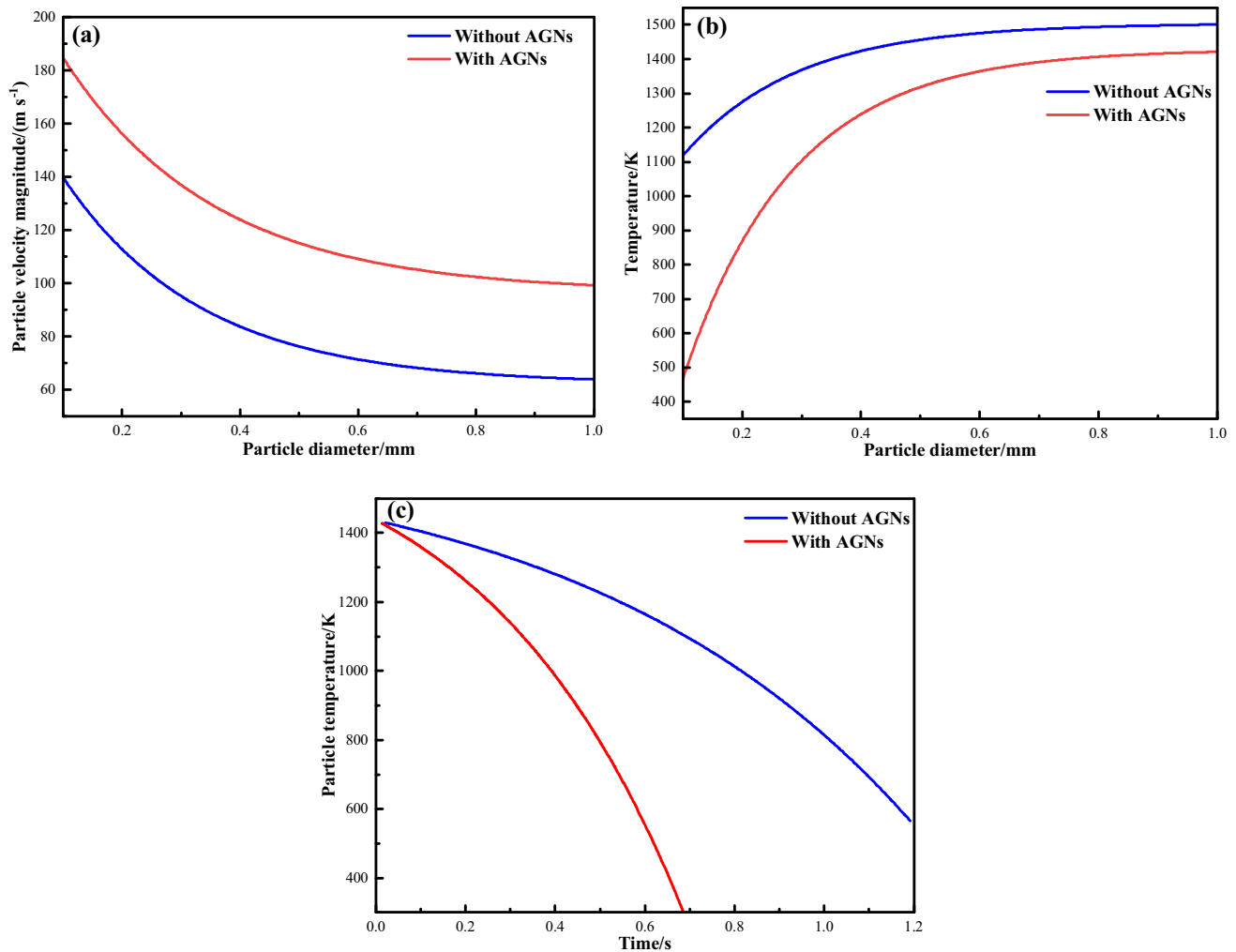


Fig. 11 Fitting curves of particle diameter and velocity (a), particle diameter and temperature (b), and particle temperature and flight time (c) under the conditions of without AGNs and with 200 m s^{-1} inlet velocity of AGNs

velocity is inversely proportional to its diameter. With 200 m s^{-1} inlet velocity of AGNs applying, the overall droplet velocities can be increased by 40 m s^{-1} , which is conducive to promoting the breakup of droplets and subsequent cooling and solidification, thereby improving the yield of fine amorphous powders [22]. It can be seen from Fig. 11b that the smaller the droplet diameter, the larger the surface area, and the higher the heat transfer efficiency between the droplets and the gas. Therefore, the droplet diameter is inversely proportional to its cooling rate, and it can be considered that the fine powder is more likely to be amorphous. After the application of AGNs, the increase in the overall droplet velocities further promotes the improvement of the cooling rate. Since the small droplets are located at the periphery of the atomizing cone and their heat transfer efficiency is much greater than that of the large droplets, the smaller the droplet diameter, the greater the increase in the cooling rate. Figure 11c is the fitting

curve of the relationship between the flight time and temperature change of the droplets captured at the outlet of the atomization chamber. With the application of AGNs, the time required for the droplets to move to the outlet is greatly reduced, and the cooling rates of the droplets are significantly improved. By extracting the data of about 50,000 particles captured at the outlet, the average and maximum cooling rates are calculated to be 2.4×10^3 and $1.9 \times 10^4 \text{ K s}^{-1}$ without AGNs, respectively, and the average and maximum cooling rates are increased to 4.1×10^3 and $2.3 \times 10^4 \text{ K s}^{-1}$ with 200 m s^{-1} inlet velocity of AGNs. The break-up of droplets is not considered in this study, so as the droplet size gradually decreases to several tens of microns, the cooling rate will further increase significantly, which means that the actual cooling rate of the atomization process equipped with AGNs will be much higher than the above calculated value.

3.4 Industrial trial results

The SEM images and size distribution of powder A and B are shown in Fig. 12a, b. Without AGNs, the median diameter of powders d_{50} of the powders is 28.42 μm , and the sphericity obtained by image processing software is 0.874; with applying 200 m s^{-1} inlet velocity of AGNs, d_{50} of the powders is decreased to 25.56 μm , and the sphericity is increased to 0.927. Combining the above simulation results, the particle dispersion angle decreases, and the collision chance between unsolidified droplets may increase, which will lead to the generation of a large number of defective powders and deteriorate the sphericity [21, 31]. However, the break-up of droplets is improved after applying AGNs, and finer droplet reduces the time required for spheroidization, which improves the sphericity eventually [32].

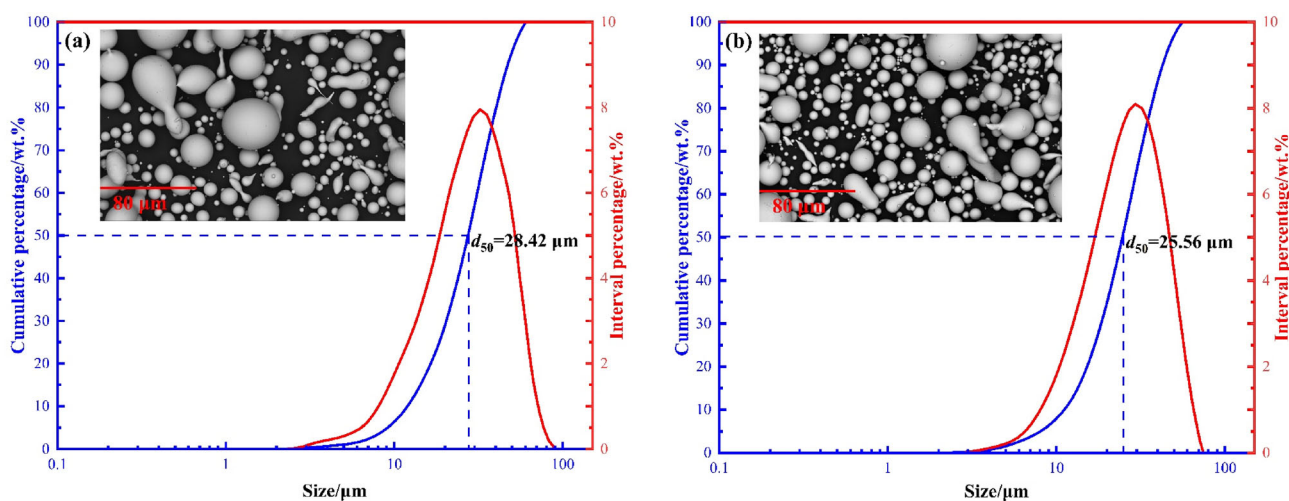


Fig. 12 SEM images and powder size distribution under conditions of powder A (a) and powder B (b)

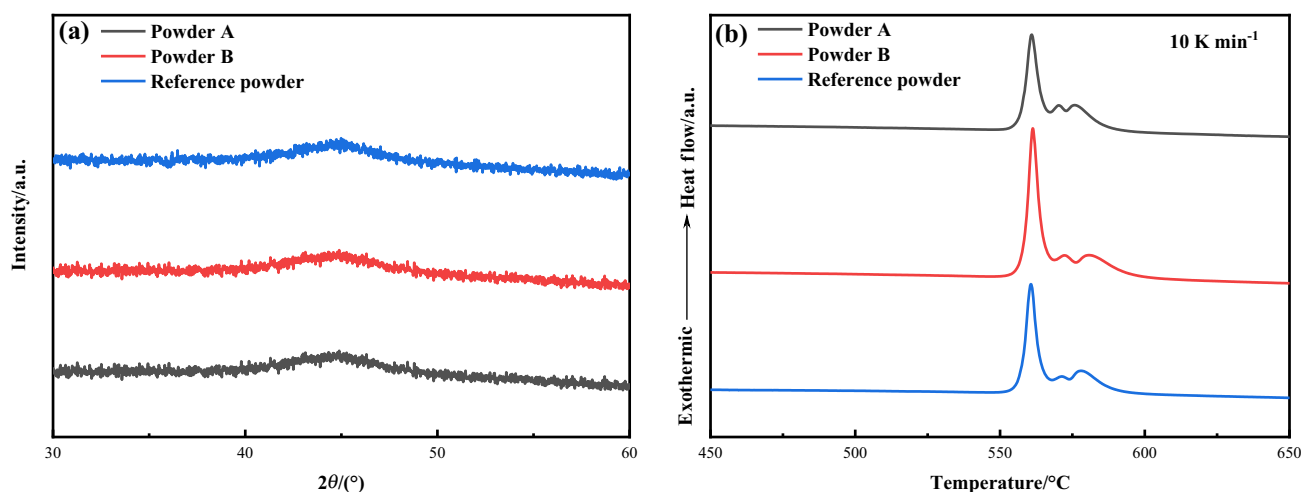


Fig. 13 XRD diffraction patterns (a) and DSC curves of three kinds of powders (b)

Figure 13a is the XRD diffraction pattern of the above two kinds of powders. The diffraction patterns both show typical amorphous broad peaks without sharp diffraction peaks corresponding to the crystal phase. The fraction of amorphous powders is quantitatively analyzed based on the crystallization enthalpy measured by DSC. The crystallization enthalpy is the energy released during the crystallization of the amorphous phase, so that a completely amorphous powder sample (of which XRD pattern is also shown in Fig. 13a) with the same composition can be selected as the reference sample, and then the ratio of the crystallization enthalpy of the above two kinds of powders to that of the reference sample can represent the fraction of amorphous phases [33]. The DSC curves of the three kinds of powders are shown in Fig. 13b, and three crystallization peaks are all formed in the range of 550 to 600 $^{\circ}\text{C}$. The crystallization enthalpies for powder A, powder B and the

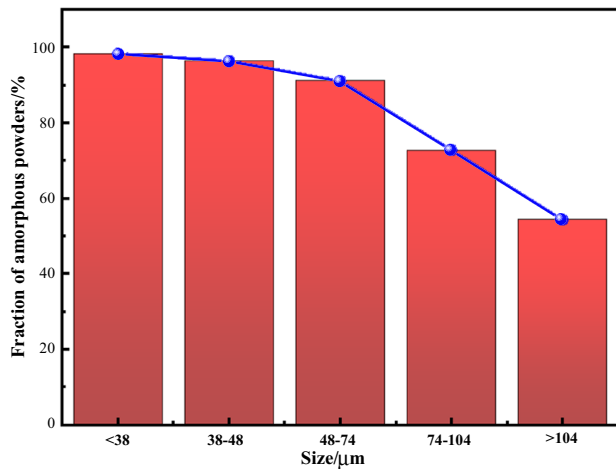


Fig. 14 Comparison of amorphous fractions of powders in different size ranges

reference sample are measured to be 111.289, 122.442 and 123.145 J g^{-1} , respectively, and then the fraction of amorphous powders A and B is calculated to be 90.4% and 99.4%.

Figure 14 shows the fraction of amorphous powders with different size ranges calibrated by the above DSC method. Powders with size smaller than 74 μm can maintain more than 90% of the amorphous fraction, and the droplet cooling rates decrease with the increase in particle size, and then the amorphous fraction decreases significantly, which effectively confirms the above simulation results. In summary, after the application of AGNs, the increase in droplet velocity and the decrease of powder size effectively increase the cooling rate, thereby greatly improving the yield of amorphous fine powders.

The hysteresis loops of powders A and B are shown in Fig. 15a, and the two loops show typical soft magnetic

properties, indicating that powders A and B both have excellent soft magnetic properties. The measurement results of saturation magnetization and coercivity are plotted as Fig. 15b, and the saturation magnetization of powders A and B are 0.85 and 0.84 T, respectively. The difference is very small, mainly because the saturation magnetization is related to the content of ferromagnetic phase. The two kinds of powders have the same composition, and therefore, the saturation magnetization is basically the same. The coercivity of powders A and B is 11.1 and 19.1 A m^{-1} , respectively. As a structure-sensitive physical quantity, the coercivity is mainly related to internal stress, impurity content and microstructure [33]. With 200 m s^{-1} inlet velocity of AGNs, the cooling rate of droplet is increased, and then the coercivity is slightly increased by the accumulation of internal stress.

According to previous studies [13, 34, 35] and the above experimental results, the size, sphericity and amorphous fraction of the powders significantly affect the soft magnetic properties of the finished electronic components. If the fraction of amorphous powders is low, the excessive precipitated crystal phases will deteriorate the permeability and coercivity; if the particle size is coarse, the high frequency core loss and direct current (DC) bias performance will be significantly deteriorated; if the sphericity is poor, it is not conducive to the subsequent insulation coating and consolidation process. Therefore, the sphericity, amorphous fraction and size of the powder prepared by the novel atomization process equipped with AGNs are significantly improved, which can provide excellent raw powders for the subsequent preparation of amorphous material parts with low core loss and excellent DC bias performance.

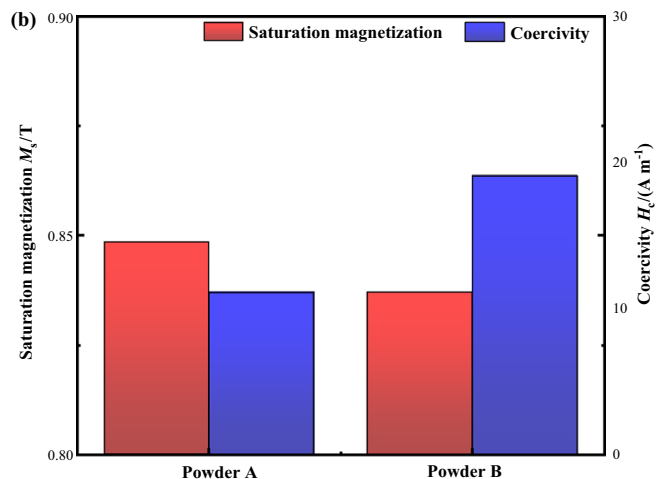
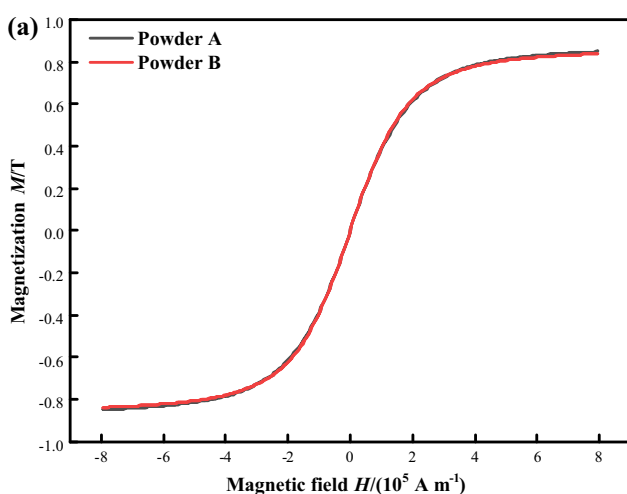


Fig. 15 Hysteresis loops (a) and comparison of magnetic properties (b) for powder A and B

4 Conclusions

1. As the atomization pressure increases from 0.5 to 3.0 MPa, the aspiration pressure gradually decreases, and the velocity of flow field gradually increases. However, the increase in atomization pressure promotes the development of oblique shocks, resulting in dramatic fluctuations of pressure and velocity, and excessive negative pressure will lead to too fast mass flow rate of melt, which is not conducive to the break-up. Therefore, an atomization pressure of 2.0 MPa in industrial production can not only effectively promote the smooth atomization, but also improve the yield of fine powders.
2. After the application of AGNs, the simulation results of the gas-only flow field show that with the increase in the inlet velocity for AGNs, the kinetic energy of the gas increases, and the velocity in the lower part of the atomization chamber increases from 45.4 to 70.4 m s⁻¹. In addition, a small pressure peak is formed below the charge nozzle, which is proportional to the inlet velocity.
3. The DPM results show that the velocity and cooling rate of small droplet are higher than those of large droplet due to larger acceleration and specific surface area. After applying 200 m s⁻¹ inlet velocity of AGNs, the overall droplet velocity is increased by 40 m s⁻¹ and the maximum cooling rate is increased from 1.9×10^4 to 2.3×10^4 K s⁻¹.
4. After the application of AGNs, the cooling rate of the droplets is increased, and the increased accumulation of the internal stress accumulation resulting in a slight increase in the coercivity of the powders. However, d_{50} of the powders is reduced from 28.42 to 25.56 μm, the sphericity is increased from 0.874 to 0.927, and the fraction of amorphous powders is increased from 90.4% to 99.4%.

Acknowledgements This work was funded by Key research and development project of Shandong province in China (Grant Number 2018TSCYCX-10).

Declarations

Conflict of interest The authors declare no conflict of interest.

References

- [1] X. Chen, B. Chen, X. Cheng, G. Li, Z. Huang, J. Iron Steel Res. Int. 27 (2020) 842–848.
- [2] F. Lu, H. Wan, X. Ren, L. Huang, H. Liu, X. Yi, J. Iron Steel Res. Int. (2022) 1322–1333.
- [3] J. Guo, Y. Dong, Q. Man, Q. Li, C. Chang, X. Wang, R. Li, J. Magn. Magn. Mater. 401 (2016) 432–435.
- [4] A. Drynda, T. Hassel, R. Hoehn, A. Perz, F.W. Bach, M. Peuster, J. Biomed. Mater. Res. A 93 (2010) 763–775.
- [5] Z. Lin, J. Zhu, J. Magn. Magn. Mater. 312 (2007) 158–163.
- [6] Z. Xiao, C. Tang, H. Zhao, D. Zhang, Y. Li, J. Non-Cryst. Solid. 358 (2012) 114–118.
- [7] A. Kus, W. Pilarczyk, A. Malachowska, A. Ambroziak, P. Gebara, Materials 14 (2021) 7357.
- [8] Y. Shi, W. Lu, W. Sun, S. Zhang, B. Yang, J. Wang, J. Mater. Sci. Technol. 105 (2022) 203–213.
- [9] S. Cardinal, J.M. Pelletier, J.C. Qiao, G. Bonnefont, G. Xie, Mater. Sci. Eng. A 677 (2016) 116–124.
- [10] H. Ding, P. Gong, K. Yao, L. Deng, J. Jin, X. Wang, Mater. Rep. 34 (2020) 139–147.
- [11] N. Zeoli, S. Gu, Comp. Mater. Sci. 38 (2006) 282–292.
- [12] W.J. Sames, F.A. List, S. Pannala, R.R. Dehoff, S.S. Babu, Int. Mater. Rev. 61 (2016) 315–360.
- [13] T. Zhao, C. Chen, X. Wu, C. Zhang, A.A. Volinsky, J. Hao, J. Alloy. Compd. 857 (2021) 157991.
- [14] Y. Liu, S. Niu, F. Li, Y. Zhu, Y. He, Powder Technol. 213 (2011) 36–40.
- [15] C. Chang, Y. Dong, M. Liu, H. Guo, Q. Xiao, Y. Zhang, J. Alloy. Compd. 766 (2018) 959–963.
- [16] X. Li, U. Fritsching, J. Mater. Process. Technol. 239 (2017) 1–17.
- [17] O. Aydin, R. Unal, Comput. Fluid. 42 (2011) 37–43.
- [18] H. Ouyang, X. Chen, B. Huang, Trans. Nonferr. Met. Soc. 17 (2007) 967–973.
- [19] D. Schwenck, N. Ellendt, J. Fischer-Bühner, P. Hofmann, V. Uhlenwinkel, Powder Metall. 60 (2017) 198–207.
- [20] J.S. Thompson, O. Hassan, S.A. Rolland, J. Sienz, Powder Technol. 291 (2016) 75–85.
- [21] P. Wang, J. Li, X. Wang, H. Liu, B. Fan, P. Gan, R. Guo, X. Ge, M. Wang, Chin. Phys. B 30 (2021) 27502.
- [22] S. Luo, H. Wang, Z. Gao, Y. Wu, H. Wang, Mater. Des. 212 (2021) 110264.
- [23] N. Ciftci, N. Ellendt, E. Soares Barreto, L. Madler, V. Uhlenwinkel, Adv. Powder Technol. 29 (2018) 380–385.
- [24] I. Ansys, ANSYS Europe Ltd, Ansys Fluent Theory Guide, USA, 2019.
- [25] F.J. Salvador, J. Gimeno, J.M. Pastor, P. Martí-Aldaraví, Int. J. Multiphase Flow. 65 (2014) 108–116.
- [26] S. Markus, U. Fritsching, K. Bauckhage, Mater. Sci. Eng. A 326 (2002) 122–133.
- [27] D. Tang, M.E. Ferreira, P.C. Pistorius, Microsc. Microanal. 23 (2017) 1082–1090.
- [28] K. Du, X. Gao, Z. Li, J. Shen, Y. Ma, Y. Hu, H. Sun, Atomization Spray. 29 (2019) 455–476.
- [29] R. Ünal, Powder Metall. 50 (2013) 302–306.
- [30] S. Motaman, A.M. Mullis, R.F. Cochrane, D.J. Borman, Metall. Mater. Trans. B 46 (2015) 1990–2004.
- [31] P. Wang, J. Li, X. Wang, B. Du, S. Shen, X. Ge, M. Wang, Chin. Phys. B 30 (2021) 54702.
- [32] O.S. Nichiporenko, Y.I. Naida, Soviet Powder Metall. Metal Ceram. 7 (1968) 509–512.
- [33] Y. Dong, J. Liu, P. Wang, H. Zhao, J. Pang, X. Li, J. Zhang, Materials 15 (2022) 1106.
- [34] C. Huang, T. Liu, X. Wang, C. Lu, D. Li, Z. Lu, J. Iron Steel Res. Int. 22 (2015) 67–71.

[35] T. Suzuki, P. Sharma, L. Jiang, Y. Zhang, A. Makino, IEEE Trans. Magn. 54 (2018) 2801705.

rightsholder(s); author self-archiving of the accepted manuscript version of this article is solely governed by the terms of such publishing agreement and applicable law.

Springer Nature or its licensor holds exclusive rights to this article under a publishing agreement with the author(s) or other